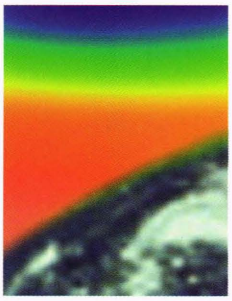

Extracting Evolving Structures from Global Magnetospheric Images via Model Fitting and Video Visualization

Christopher J. Chase and Edmond C. Roelof

Global images of magnetospheric ion populations can be produced for both extreme ultraviolet (EUV) photons and energetic neutral atoms (ENAs). The development of instrumentation for magnetospheric imagery and the design of future missions demand realistic simulations of emissions from magnetospheric ion populations. When EUV and ENA cameras are actually flown in space, inversion of the images obtained will provide the physical parameters describing ion populations. Using ion distribution models, we generate simulated images that incorporate the global dynamics of the magnetosphere. These images reveal the global morphology of magnetospheric ion populations, and video presentation of image sequences portrays the complex evolution that magnetospheric ions undergo during disturbed geomagnetic conditions.

INTRODUCTION

The magnetosphere can be thought of as the region of space surrounding the Earth that is filled with magnetic field lines passing through the Earth's surface (or, more strictly, through the ionosphere that lies several hundred kilometers above the Earth's surface). If the field lines close, they trap charged particles, which then bounce back and forth from one end of the field lines to the other in mirroring orbits. Such field lines form the Van Allen radiation belts of very energetic ions and electrons, as well as a region called the ring current, which fills up with energetic ions during geomagnetic storms that disturb the field lines. A stable, but much less energetic region of "cold" plasma drawn up into the magnetosphere from the ionosphere is called the plasmasphere. The bulk of the ring current usually lies outside of the plasmasphere, but the two populations often overlap. These two regions are of great interest because they are laboratories for the study of cold and hot trapped plasmas and their mutual interaction. We can now image these important ion populations of the magnetosphere, and we will explore methods for extracting physical information from magnetospheric images.

MAGNETOSPHERIC IMAGING

The current knowledge of the magnetosphere is based on *in situ* spacecraft measurements and ground observations from the last three decades. However, this information provides a very incomplete picture of the

global nature of the magnetosphere because of the many complex and distributed processes that play a role in its dynamics. Indirect measurements of the global magnetosphere would be invaluable in increasing the limited information obtained so far.

Global imaging of the magnetosphere is possible via two experimental techniques: extreme ultraviolet (EUV) imaging and energetic neutral atom (ENA) imaging. Both types of observations have already been obtained from crude imaging experiments, such as He^+ images from Space Test Program 72-1[1] and ENA (>25 keV) images from International Sun–Earth Explorer–1.[2] Although these images did not contain detailed information on the magnetosphere, they served as proof-of-concept experiments to support the type of imaging we envision. The focus of the work described in this article is ENA imaging, but the techniques also apply equally to EUV imaging.

ENA imaging measures the fast neutral atoms produced when singly charged energetic ions have a charge-exchange interaction with the cold hydrogen atoms of the Earth's exosphere. The ions gyrate as they move along the magnetic field lines. These ions bounce back and forth between mirror positions on the field lines until they encounter an exospheric hydrogen atom. The ion becomes a fast neutral atom when it strips an electron from the hydrogen and then is no longer confined along the magnetic field lines. Because of the very high energy of the ion, it continues along the same path that it had at the instant of the interaction with essentially no loss in energy. Magnetospheric ENA emissions are optically thin, that is, we can ignore absorption due to reionization between the source and the observer. Thus, the stream of neutral atoms reaching an observer along some line of sight is a simple sum of all fast neutral atoms produced along that line that are directed back toward the observer.

The ENA emissions can be detected with a sensitive energetic particle detector that uses electrically charged plates to reject the local energetic ions. Such an instrument is effectively an ENA camera. The ENA camera images the energetic (>1 keV) ions that populate the so-called ring current and plasmasheet regions of the magnetosphere. Technical details of ENA imager designs can be found in Keath et al.,[3] Hsieh and Curtis,[4] and McComas et al.[5] It should be noted that an ENA imager is actually a particle counter within discrete angular sectors rather than an optical telescope collecting scattered photons from sunlight, as happens with EUV imaging.

IMAGING FUNDAMENTALS

The concepts of magnetospheric imaging and their historical development over the past 20 years may be found in two recent review articles.[6,7] A model for EUV or ENA imaging begins with the intensity impinging upon an instrument at position $\mathbf{r}$ from a direction $\mathbf{u}$ of photons at wavelength λ or ENAs with energy E. The relationship between the EUV irradiance $4\pi I$, measured in Rayleighs (10^6 photons·cm^{-2}·s^{-1}), and the density n_{atom} of the atoms (which may be ionized) involves the g-function, which gives the number of solar photons resonantly reradiated per second by each atom at wavelength λ. In the simplest case, the g-function depends only on the electronic structure of the atom and the intensity at the center of the solar line. This relationship holds true only when the reradiating atoms have relatively small thermal velocities, that is, when the solar line, which has a finite width, is not appreciably Doppler shifted in the atom's rest frame. The relationship between the ENA unidirectional differential intensity j_{ENA} (cm^2·sr·s·keV)$^{-1}$ at an energy E and the corresponding energetic ion intensity j_{ION} involves the energy-dependent charge-exchange cross section σ (cm^2) and the exospheric H-atom density n_H. The cross section can be interpreted as the probability of a charge exchange occurring.

In the "optically thin" case where we can neglect any reabsorption of the EUV photon or the ENA between the emission point and the spacecraft, the measured intensities may be expressed as line integrals over the emissions:

$$4\pi I_{EUV}(\mathbf{r}, \lambda, \mathbf{u}) = g(\lambda) \int_0^\infty n_{atom}(\mathbf{r} - \mathbf{u}s)\, ds\,, \qquad (1)$$

$$j_{ENA}(\mathbf{r}, E, \mathbf{u}) = \sigma(E) \int_0^\infty n_H(\mathbf{r} - \mathbf{u}s) j_{ION}(\mathbf{r} - \mathbf{u}s, E, -\mathbf{u})\, ds\,. \qquad (2)$$

The line integrals run from the spacecraft position $\mathbf{r}$ to ∞ along the look direction $(-\mathbf{u})$ opposite to that of the arriving EUV photon or ENA. Comparing Eq. 1 with Eq. 2, one sees that the ENA inversion problem is usually the more complex one. However, if the EUV reradiation comes from atoms with relatively large thermal velocities such that some atoms "see" the solar photons significantly Doppler shifted, then the EUV inversion is even more complex than the ENA inversion because the atom velocity distribution at each point along the line of sight must be convolved with the shape of the solar line. This inversion is too complicated for us to explore in this article. Consequently, for the remainder of the article, we shall discuss the general ENA problem of Eq. 2. The reduction to the simplest EUV case ("cold" atoms) described by Eq. 1 is obvious: simply set j_{ION} in Eq. 2 equal to a constant, and let n_H have the spatial dependence of the EUV-emitting atoms.

The energy dependence of $\sigma(E)$ is critical in ENA imaging. Its value is about 10^{-15} cm^2 at E = 10 keV for both energetic H^+ and O^+ incident on neutral H. However, the value plummets to 10^{-17} cm^2 for 100-keV protons, whereas it drops by only a factor of 2.5 down to 4×10^{-16} cm^2 for 100-keV O^+. The spatial dependence of $n_H(\mathbf{r})$ was measured over a 4-year period by the far-ultraviolet imager on the DE-1 spacecraft.[8] The exospheric H-atom density $n_H(\mathbf{r})$ is generally stable at high altitudes and approximately spherically symmetric. It falls off montonically like a Chamberlin-model exosphere,[9] having a density of 44,000 cm^{-3} at the exobase (top of the atmosphere), about 10^3 cm^{-3} at a radial distance of 2 Earth radii (R_E = 6370 km), and about 10 cm^{-3} at 12 R_E.

The ENA intensity $j_{ENA}(\mathbf{r})$, as measured from a spacecraft at position $\mathbf{r}$, varies with time for two reasons. First, the ion populations within the magnetosphere can be very dynamic during and immediately after a solar disturbance. Second, $\mathbf{r}$ varies as the instrument moves along its orbit. Indeed, the separation of spatial gradients from temporal evolution has plagued the reconstruction of global phenomena using conventional *in situ* measurements of local fields and particles. The problem is much less severe with magnetospheric imaging because the cameras see most of the magnetosphere at any given time.

IMAGE SIMULATION

Modeling and simulation of ENA imaging serves three purposes. First, it helps to make foreground estimates of j_{ENA}, which are essential for ENA imager design. Second, it allows us to anticipate the potential information that ENA images contain on the global distribution of ion intensities, j_{ION}. ENA images are very rich in information because separate images can be obtained at many energies over a large energy range (0.1–100 keV) and for several species of singly charged ions; H^+, He^+, and O^+ are the most abundant in the Earth's magnetosphere. Third, modeling and simulation of ENA imaging allows us to learn how to extract the global morphological information about magnetospheric dynamics, which is unavailable via *in situ* measurements. In the next three sections, we will discuss these purposes of image modeling and simulation.

An actual image is obtained by convolving j_{ENA} with the instrument response function and integrating the output over the instrument sampling period. The combination of the instrument response and the sampling integration can be approximated by a tent-like function over a two-dimensional window (over the space for the look direction $\mathbf{u}$) that multiplies j_{ENA} and then is integrated for each image pixel. For an ideal instrument with a very high resolution and a short sampling period relative to the changes in the viewpoint as the instrument spins and moves along its orbit, the resulting window is approximately a delta function. In this article, we will treat the sampling window as a delta function that builds up the ENA image by sampling j_{ENA} on a grid corresponding to the angular resolution (i.e., the window size) of the instrument. See Ref. 2 for an example of interpreting an actual instrument response function.

Simulating the imaging process requires reasonable models of the ion population, j_{ION}, in Eq. 2. Typically, models express j_{ION} as a function of L, the radius in R_E of a given magnetic field line where it crosses the magnetic equator. For a dipole field (a good approximation to the Earth's field at high altitudes), L is a constant along a magnetic field line. The intensity j_{ION} is strongly attenuated inside $2R_E$ by charge-exchange losses (the very process that generates the ENA), so it peaks around L = 4 and then decays approximately exponentially with increasing L. Consequently, ENA images are brightest in the inner portions of the magnetosphere, particularly at low altitudes where the magnetic field lines approach the Earth (because the exospheric H-atom density increases rapidly with decreasing altitude). However, imaging cameras can be designed to have sensitivity sufficient to measure ENA intensities to the outer edge of the ion trapping region ($L \cong 10$).

Many researchers have fit various parametric models to synoptic *in situ* measurements of the ion intensity j_{ION} by combining intensities measured by the same spacecraft over many orbits but sorted into bins according to the level of magnetic activity. Alternatively, nonparametric theoretical models that inherently contain the basic physics of the dynamics of the ion distributions can now be generated by computer codes that track plasma motions in electric and magnetic fields. In these plasma simulations, the fields are deduced from synoptic observations sorted into bins by magnetic activity. In particular, we mention the highly complex Rice Convection Model[10] and its somewhat simplified derivative, the Magnetosphere Specification Model (MSM). These two models, developed at Rice University, calculate the electromagnetic field and plasma distribution function in the magnetosphere self-consistently by using multi-fluid magnetohydrodynamical equations with the observed magnetic activity indices as input. Using the MSM model, we have been able to obtain simulated images giving insight to potential information that can be provided by future imaging missions.

FOREGROUND ENA ESTIMATES

The optically thin characteristics of ENA images of three-dimensional ion distributions are much more difficult to visualize than images from space of the two-dimensional aurora or cloud patterns above the Earth's

surface. Consequently, images of the complex three-dimensional structure of the ENA emissions exhibit considerable variation in intensity and configuration, depending on the viewing vantage point, so that computer simulation of these images has proved indispensable in setting design requirements for ENA cameras. Even the estimation of the brightest region in an image is difficult because of the complex geometry of the ion distribution. These simulations use models of ion distributions, as discussed previously. Our calculations are normalized absolutely by the ENA measurements[2] from the ISEE-1 spacecraft, which showed that, during a major geomagnetic storm, the maximum intensity for either 25–35 keV H or 60–77 keV O would be on the order of 10^3 $(cm^2 \cdot s \cdot sr \cdot keV)^{-1}$.

From sets of simulations for different vantage points, we have extracted the characteristic ranges of intensities (within an order of magnitude) to be expected during an imaging mission. These intensities are classified according to characteristic structural regions that have been identified in past ground-based and *in situ* measurements, for example, ion-injection boundaries during geomagnetic storms. Assuming a low instrument background, we calculated that for the 25–35 keV H ENAs, 1% intensity variations during 5 min in the heart of the storm-time ring current could be detected within a 1-R_E region from a distance of 5 R_E. Although we calculated that it would be difficult to sense remotely 10–20% intensity variations within the outermost trapping region of this energy band during a 5-min exposure, they may be more easily measured for lower energy (1 keV) ENAs.[5] Besides assisting in instrument design, ENA images can provide quantitative information about the magnetosphere, which we discuss next.

EXAMPLE OF AN ENA IMAGE

We show each ENA image as a pinhole representation, sometimes called a fish-eye view, which is the same way that the human eye perceives an image. The pinhole representation is of the line-of-sight intensities projected on a hemisphere of normalized radius. As such, an ENA image can be thought of as a polar intensity plot where the radial distance from the center of the image is proportional to the polar angle measured from the view axis, and the clock angle is an angle measured in some plane perpendicular to the view direction (e.g., one that contains the magnetic north direction).

Figure 1a is an example of a pinhole ENA image. It is calculated from an MSM run using as inputs the observed magnetic activity indices measured during the magnetic storm of 22–23 May 1988. The instrument response is emulated by sampling the image on a 2 × 2° grid and representing the value as a 2 × 2° pixel. The view is near-polar from about 7.9 R_E and 79° magnetic latitude above the dawn meridian looking directly at the Earth's center. The Sun is therefore to the right. The white circle is the Earth's limb. North is toward the top of the image, and dusk is on the left. The intensities at the outer edge are 90° from the viewing direction. The black patch in the center is over the north magnetic pole where the magnetic field lines are open, so no significant ENA intensities are found there. The most intense regions surround the hole at the North Pole at low altitudes, where the exospheric neutral hydrogen density (n_H) is the highest, thus producing the highest ENA intensities j_{ENA} according to Eq. 2. The ENA intensities are highest on the nightside and weakest on the dayside during periods of high activity because ions are energized on the nightside and then drift around to the dayside as a result of the combined effects of the disturbed electric field and the dipole-like confining magnetic field. The nearly circular outer boundary of the image is an artifact of the MSM model; no ion intensities are calculated outside of $L = 9$.

MEASUREMENT UNCERTAINTY

Noise in actual images is due in part to instrument background, but it is usually dominated by the variations in the counts of the arriving ENA particle intensity at the instrument. These counting statistics are well modeled by a Poisson point process. Given the mean number of counts λ expected in a given time interval for a particular look direction $\mathbf{u}$ and position $\mathbf{r}$, the probability distribution of observed counts n is $P(n; \lambda) = (\lambda^n e^{-\lambda})/n!$ for $n = 0, 1, 2, \ldots, \infty$. When the mean number of counts exceeds a moderate size (>20), the counts approach a Gaussian distribution with mean $\langle n \rangle = \lambda$ and standard deviation $\sigma_n = \lambda^{1/2}$. Furthermore, statistical variations in different pixels are independent; that is, spatially the Poisson variations are statistically uncorrelated or "white." To simulate a noisy image, we compute the number of counts that would be sampled in a given pixel by the instrument during an exposure time Δt for an intensity j_{ENA}, which is the expected number of counts λ for that image pixel, and then assign each pixel a random number n selected from the associated Poisson distribution $P(n; \lambda)$.

To illustrate the effects of counting statistics on an image, we take the ENA image simulated for 30-keV proton intensities from the MSM shown in Fig. 1a, and we introduce the Poisson fluctuations that would occur in a finite exposure time by varying the expected number of counts n in the brightest 2 × 2° pixel. Figures 1b, 1c, and 1d represent images with peak pixel counts of 1000, 100, and 10, respectively, which therefore have >3%, >10%, and >30% uncertainty in the brighter pixels and much greater uncertainty in the dimmer pixels. The image degradation is minimal in Fig. 1b,

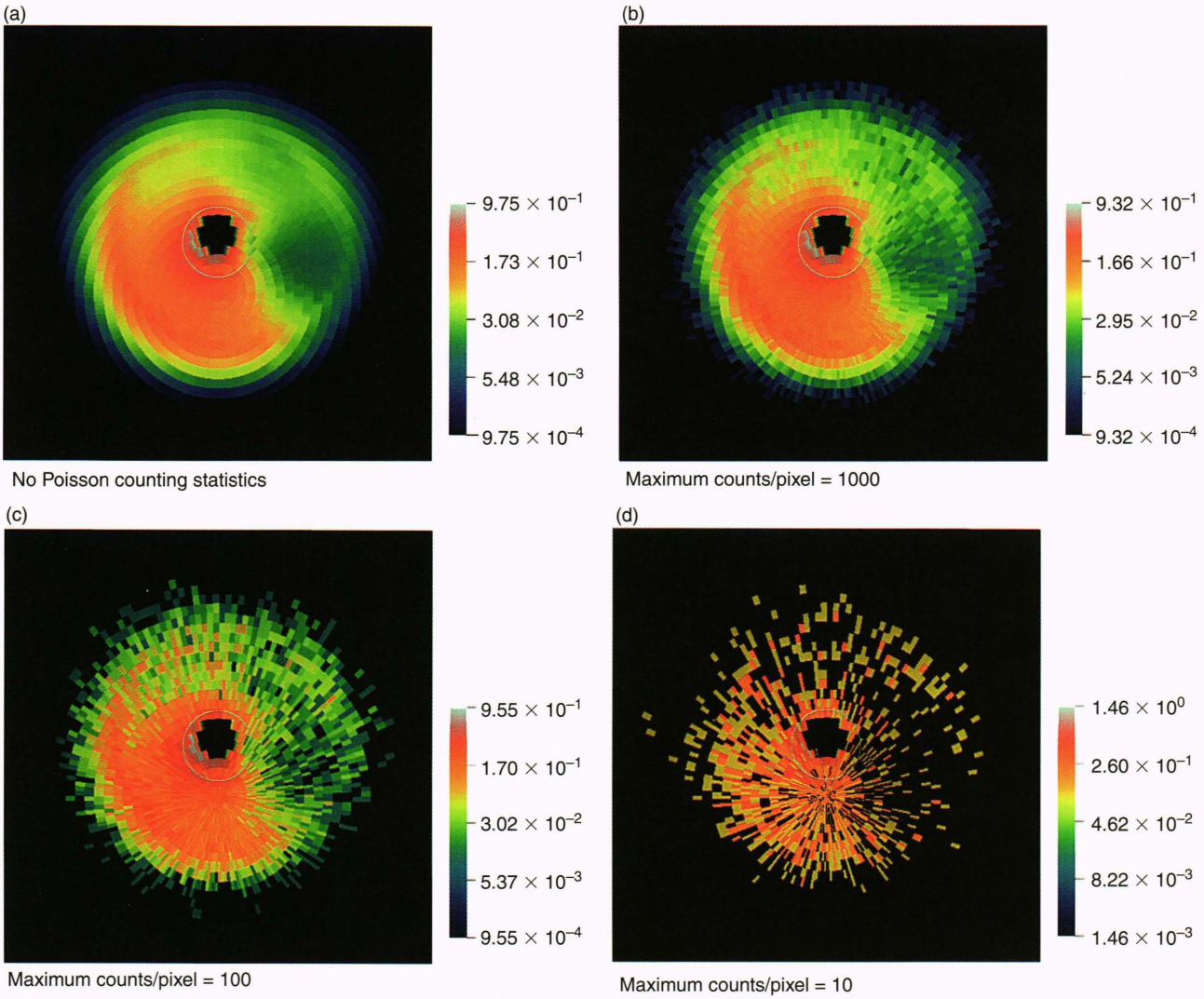

Figure 1. Simulated ENA images of 30-keV H^+ from 7.9 R_E and 79° latitude, generated with 2 × 2° angular resolution. (a) No Poisson counting statistics. (b)–(d) Effects of Poisson counting statistics for total counts of 1000, 100, and 10, respectively, in the brightest pixel. Note that even with only 10 counts in the brightest pixel, large-scale morphology is still evident. The color bars are logarithmic, covering a factor of 1000 in intensity, normalized to the brightest pixel.

and even in the highly degraded image of Fig. 1d, the general morphology is still evident (intensity deficiency on the dayside compared with the nightside).

EXTRACTION OF ION INTENSITY FROM AN ENA IMAGE

The power of magnetospheric images lies in their ability to display the global morphology of magnetospheric processes immediately, that is, the where and when. The images also contain quantitative information on a global scale. In principle, such global information could be gathered from many *in situ* spacecraft making point measurements, but the number of such spacecraft required would be impracticably large (>1000).

Although the advantages of global imaging over *in situ* sampling are many, the extraction of relevant magnetospheric information from global images is still a challenging task. Recall that the images are fundamentally composed of integrals along the lines of sight from the observation point given in Eq. 2. Ultimately, given measured images from future experiments, we want to extract or "unfold" features of the distribution of ion intensities j_{ION} in Eq. 2. This is an inversion problem similar to those commonly encountered in remote sensing experiments. Indeed, inverting this integral equation bears similarity to tomographic techniques. In tomography, many scans of an object are made from a large number of vantage points that essentially cover the entire space of possible vantage points. It is required that the scanned object not change during these scans

and that the radiating source be known exactly. In magnetospheric imaging, the time scales during which the magnetospheric structures evolve are generally much shorter than the orbital period of the spacecraft. Additionally, a calibrated source is not an inherent parameter. Thus, tomographic inversion techniques are not applicable.

Instead of tomographic techniques, we have used techniques that fit a parameterized model of the magnetosphere to the measured images. The parameters of the model we have implemented describe important salient morphological features of j_{ION}, such as inner and outer boundaries of the magnetosphere and the variations of these boundaries with respect to magnetic local time (analogous to the geographic longitude but with respect to magnetic north).

FORWARD INVERSION THEORY BASICS

Strictly speaking, image inversion would involve working backwards from data to obtain the model parameters. However, a more useful approach in our case incorporates a technique well known in astronomy and astrophysics: it involves adjusting the parameters of the model and working forward by iteration until the parameters fit the data. Such forward inversion methods attempt to estimate the model parameters that provide a best fit between simulated model data and the measurements. Typically, the criterion for measuring the goodness of the fit can be expressed as a scalar function of the model output and measurements. This function is called an error function because it measures the error between the model and measurements.

One typical criterion for the fit is choosing the parameters that maximize the probability, or likelihood, of the measurements for the selected parameters. For our problem, the probability of the measurements is characterized by the Poisson statistics included in the imaging model. This method of parameter estimation is called the maximum likelihood estimate. Another criterion is the least-squared error, and the corresponding technique is called least-squared-error estimation. It finds the model parameters that minimize the sum-squared difference between the measurements and the model data. A variation of this method is the weighted least-squares estimate, which multiplies the squared difference error for each data point by an associated weight before summing. A specific example of this is the chi-squared measure of goodness of fit. When the mean counts are large enough that they have Gaussian statistics, the maximum likelihood estimate is well known to be equivalent to the weighted least-squared-error estimate, where the weights are the reciprocals of the variance at each measured image pixel. In this case, the error function is the same as the chi-squared measure. In addition, other criteria besides the maximum likelihood estimate and weighted least-squares estimate are used for evaluating good fits.

Two important difficulties are encountered in forward inversion problems. First, the number of measurements may be so few as to make the inversion problem indeterminate. In other words, there just are not enough measurements to distinguish the parameters. Sometimes, the problem remains indeterminate no matter how many measurements are taken. In this case, a different model is probably more relevant to the measurements. Second, the inversion problem may be ill-conditioned. In this case, the model may not be sufficiently constrained, resulting in an unstable inversion. Unstable means the inversion is very sensitive to small perturbations in the measurements. One cannot have very much confidence in the estimates returned from an unstable inversion.

FORMULATION OF A PARAMETER EXTRACTION TEST

For our problem, a large number of measurements are available, and the parametric model we use is highly constrained. For our data, we use images simulated from the ion intensities generated from the MSM runs. These are stand-ins for the actual ENA images we hope to obtain from future magnetospheric imaging missions. For the parametric model to be fit to the simulated data, we choose a simple model for the distribution of ion intensities j_{ION} that characterizes the large-scale morphological features of the magnetosphere according to observations from past experiments. By attempting to fit only these large-scale features, our model overcomes some of the inversion difficulties mentioned previously.

The functional form of the ring-current energetic ion intensities that we chose for this initial attempt at automated image unfolding involves 10 parameters. The two variables are L (constant along a dipole field line defined in spherical polar coordinates by $r = aL\cos^2\Lambda$, where $a = 1R_E$ and Λ is the geomagnetic latitude) and the azimuthal angle ϕ, measured anticlockwise from the sunward direction, so that $\phi = 0$ (the $+x$ axis) is 1200 magnetic local time (MLT), $\phi = 90°$ (the $+y$ axis) is 1800 MLT, etc. Then we write

$$j_{ION} = j_0 \exp(-F_\phi - F_L) . \qquad (3)$$

The exponential form is chosen for j_{ION} because the observed intensities vary far too strongly to be described by linear expansions; this form rules out many of the techniques of image inversion that rely on linear algebra. For the ϕ dependence, a harmonic expansion is convenient:

$$F_\phi = k_1[1 - \cos(\phi - \phi_1)] + k_2[1 - \cos 2(\phi - \phi_2)] \,. \quad (4)$$

A second harmonic expansion of F_ϕ allows us to modulate the intensity in MLT so that we can have a region of maximum ion intensity, which is observed on the nightside of the Earth, as well as a dawn–dusk asymmetry, which is also observed. For the L dependence, synoptic data compilations suggest the following:

$$F_L = \begin{cases} (L - L_1)^2 / 2\delta L_1^2 & L < L_{11} \\ (L - L_{11}) / L_0 + (1/2)(\delta L_1 / L_0)^2 & L_{11} \le L \le L_{22} \\ (L - L_2)^2 / 2\delta L_2^2 + (L_2 - L_1)/L_0 \\ \quad + (1/2)(\delta L_2 / L_0)^2 - (1/2)(\delta L_1 / L_0)^2 & L > L_{22} \end{cases} \quad (5)$$

where $L_{11} = L_1 + \delta L_1^2 / L_0$ and $L_{22} = L_2 + \delta L_2^2 / L_0$ mark the L values where j_{ION} changes smoothly (with continuous slope) from a Gaussian to an exponential ($L = L_{11}$) and from an exponential to a Gaussian ($L = L_{22}$). In our simplest models, all the coefficients in F_ϕ and F_L are constants, so that j_{ION} is a separable function of L and ϕ. However, since the problem is already nonlinear, separability does not simplify the inversion problem that much. There is no reason not to allow F_ϕ to change its shape with L, if k_1, ϕ_1, k_2, and ϕ_2 are allowed to depend on L. Likewise, some ϕ dependence can be permitted in the parameters of F_L (L_1, δL_1, L_2, δL_2, and L_0). Figure 2 shows plots of the surface j_{ION} (L, ϕ) from four perspectives in which the x and y axes are rotated 90° in each successive plot. Parameter values used to generate the surface are given in Fig. 3.

Our initial investigations have been with constant coefficients in Eqs. 3 through 5. Then the inner and

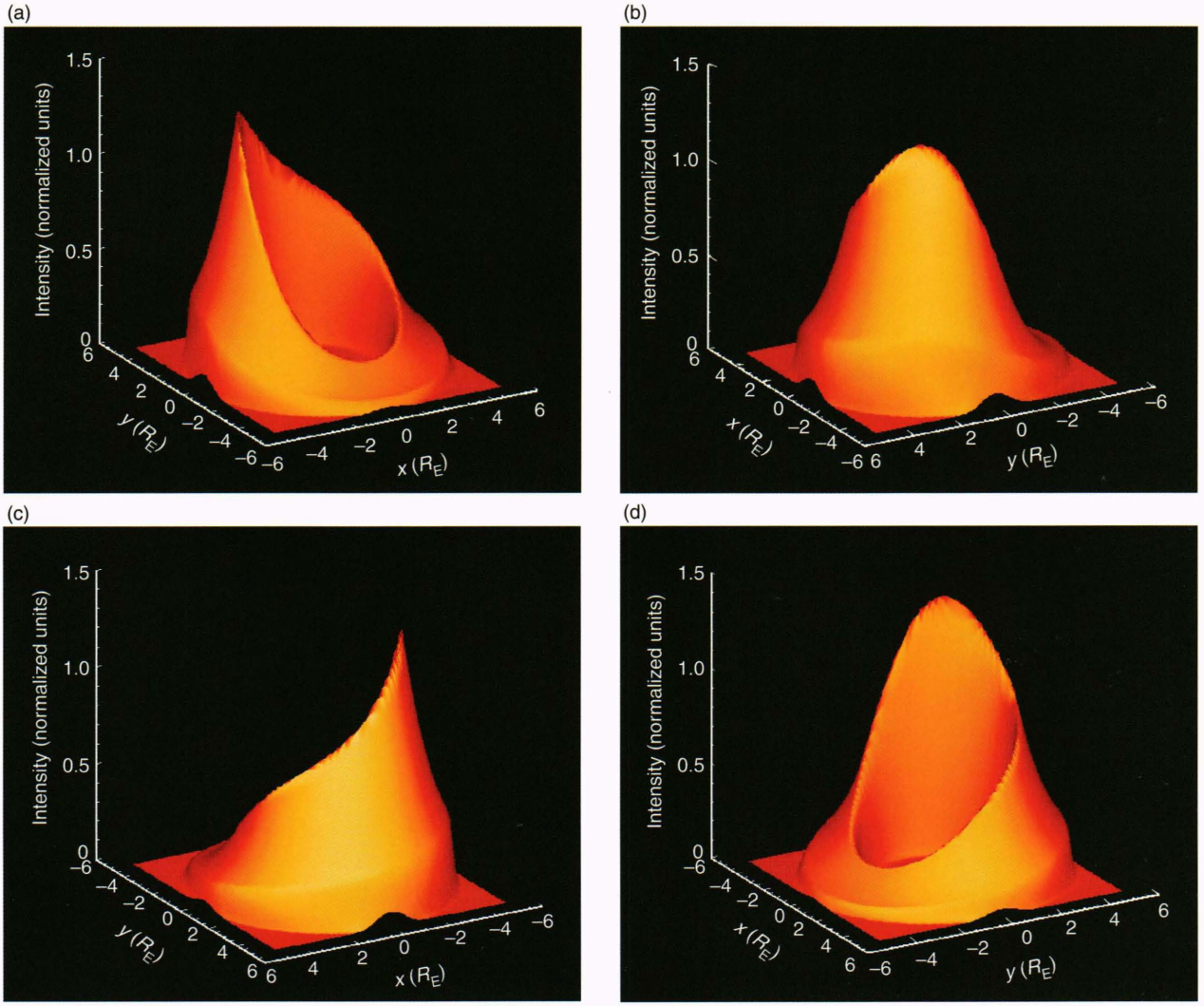

Figure 2. Ten-parameter model for the global spatial dependence of ion intensity to be used in a test against the nonparametric Rice University MSM plasma computer code. The surface representing j_{ION} (L, ϕ) from Eqs. 3 through 5 is shown from four perspectives, each rotated by 90°.

outer transition L values (L_{11} and L_{22}) are constant, so the boundaries of the ring-current distribution are quasi-axisymmetrical. This model has its limitations, but because of the MLT modulation in F_ϕ, it still has considerable flexibility in describing the gross morphology of the high-intensity regions of the ring current. The model contains 10 independent parameters: the absolute normalization of the ion intensity j_0, the two amplitudes and two phases in F_ϕ, and the linear scale (L_0) and two pairs of Gaussian parameters (L_1, δL_1, L_2, δL_2) in F_L.

OPTIMIZATIONAL APPROACHES

For a given error function, an optimal parameter estimate is one that minimizes the error function. The error function minimum cannot be found directly except when the model is linear in the parameters (e.g., a polynomial fit in regression analysis). If the error function is nonlinear, the minimum must be solved for by an iterative process. In our case, the model is always nonlinear, which leads us to using an iterative method of minimizing the error function. Many well-known minimization algorithms are available for this task.

Several issues affect the effectiveness of a chosen minimization algorithm for solving the inversion problem. Some of these are (1) the number of parameters, (2) the computational expense of computing the model, (3) the nonconvexity of error (i.e., the presence of many shallow local minima in the objective function), and (4) parameter constraints. Issues 1 and 2 affect the length of time required by a minimization algorithm to find a solution. Because there are practical bounds on how long we are willing to wait to find a solution, it may be important, depending on the minimization algorithm chosen, to limit the number of parameters and the number of model evaluations. Issue 3 affects the ability of many algorithms to find the best answer to the inversion problem, and issue 4 may not be applicable to many types of algorithms or may be difficult to implement.

Optimization algorithms can be either derivative or nonderivative techniques. Derivative techniques converge faster to a solution but require direct computation of the objective function derivative. In many problems, such as ours, the derivative cannot be computed directly but must instead be approximated by using finite-difference formulas. Derivative techniques often use a steepest descent to move "downhill" in the direction of the gradient, or they attempt to approximate the objective function locally as a quadratic surface in the parameter space and step toward the approximated minimum directly. Stochastic analogs of these algorithms, for example, simultaneous-perturbation stochastic approximation,[11] attempt to avoid the large number of forward-model calculations incurred by finite-difference methods in estimating the gradient data as the algorithm steps along its search path.

Some nonderivative methods attempt line searches over a spanning set of directions. These nonderivative methods are very slow, requiring large numbers of steps to converge to a minimum. If computation of the forward model and thus the objective function involve many operations, then these methods are extremely time-consuming. Common examples of these methods are the Powell conjugate direction algorithm, the downhill simplex, and simulated annealing. Simulated annealing is actually a statistical algorithm that can take random steps that increase the objective function. The advantage is that simulated annealing can avoid local minima at a cost of much slower convergence.

To date, we have only used versions of the Powell algorithm for inversion of ENA images. Because our model can contain 20 to 30 parameters, depending on the order of the harmonic expansions used, and because the exponential-like line integrals of the forward model can be computationally expensive, our inversion algorithm is very slow. We provide an example in the next section. We have begun to investigate other techniques that may be more robust to initial conditions, for example, the downhill simplex, or faster in requiring fewer evaluations of the forward model, for example, the stochastic approximation method.

RESULTS OF A PARAMETER EXTRACTION TEST

In this section, we give an example of ENA image inversion.[12] The data image was generated nonparametrically from the Rice MSM model for 30-keV protons (H^+), which, in this case, simulates the main phase of the geomagnetic storm in May 1988. Another (more polar) ENA image of the same storm-time ion distribution was shown in Fig. 1a. Figure 3a shows a pinhole view of the data image from about 3 R_E at 60°N geomagnetic latitude in the dawn meridian looking at the center of the Earth. North is toward the top center, and the white circle defines the Earth's boundary. The color bar shows the normalized ENA intensities on a linear scale. The intensities for the image were generated on a $4 \times 4°$ grid.

We note the obvious buildup in the image on the nightside as expected, whereas excess intensities in the dusk sector might actually be due to deceptive line-of-sight projection effects. By inspection, we can estimate the outer extent of the protons at roughly 4 R_E. However, the inner extent of the protons is impossible to deduce without image inversion because that region is obscured by emissions from protons on field lines farther out than the innermost one. Our example inver-

sion demonstrates that gross morphological properties such as the inner boundary of the protons can be quantitatively extracted from the image.

In this example, we used the Powell minimization method to determine the least-squared-error estimate for the ion intensity parameters based on the 10-parameter version of j_{ION} given in Eqs. 3 through 5. Using an unweighted least-squared-error function favors fitting our intensity model more closely to the brighter regions of the image. The inversion required 216 evaluations of the forward model over three complete iterations of the Powell algorithm (an iteration consists of line search minimizations over a spanning set of directions in the parameter space).

Figure 3b is the simulated ENA image reconstructed using the estimated parameters returned by the image inversion. Notice that the shapes of the brightest regions in both images are very similar and that their

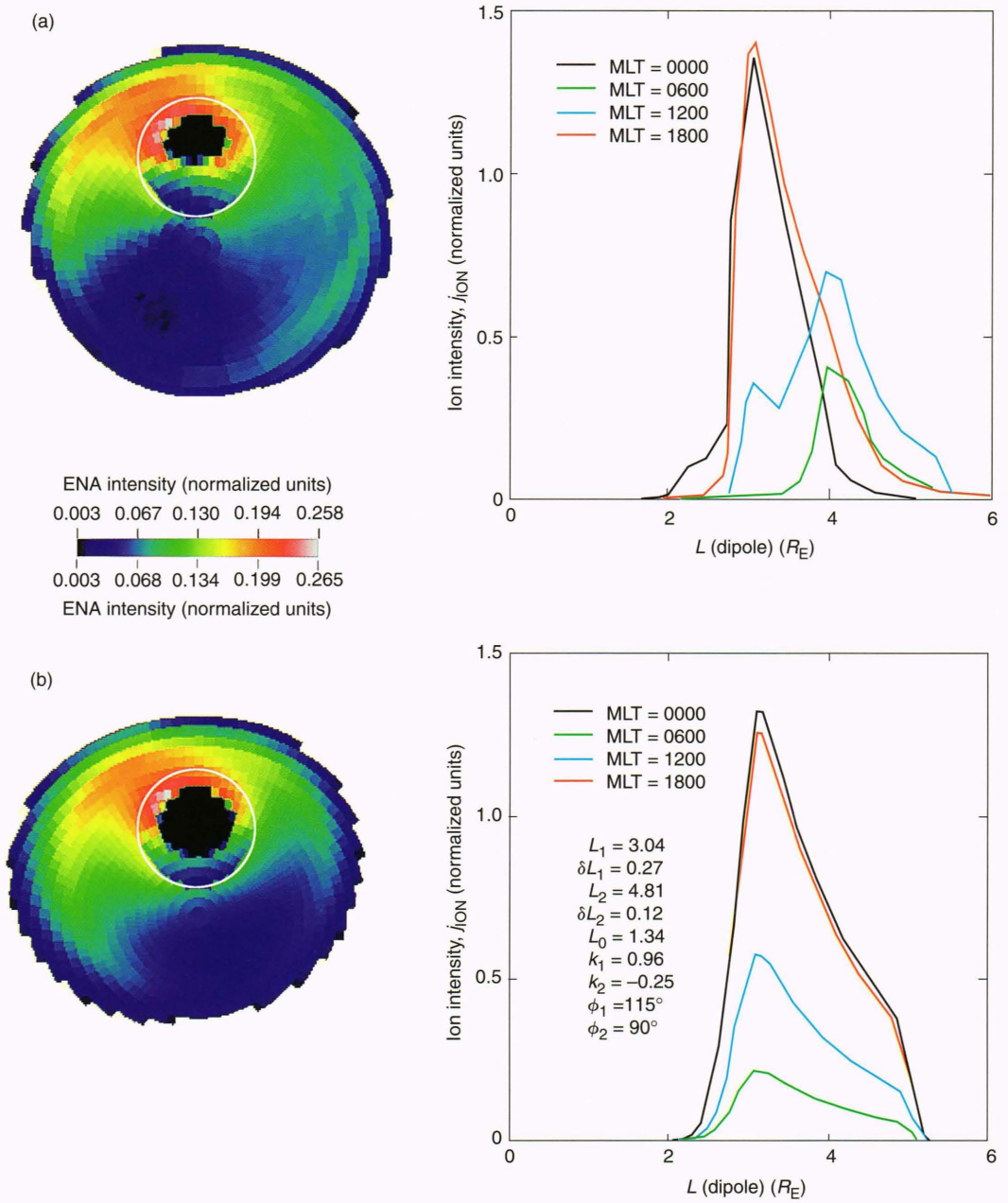

Figure 3. (a) ENA "data" image from 3 R_E and 60° geomagnetic latitude simulated from a 30-keV H^+ distribution derived from a nonparametric MSM run using inputs from the geomagnetic storm of 22–23 May 1988. The color bar is logarithmic (factor of 100). (b) ENA image reconstructed from an optimal set of 10 parameters extracted by optimizing the fit to the model given by Eqs. 3 through 5. To the right of each image are corresponding plots of j_{ION} versus L for four magnetic local times. Note the general agreement of peak ion intensities at all magnetic local times. (Adapted from the analysis of Roelof et al.[12])

absolute magnitudes, as indicated by the maximum of the color bar, are very well reproduced. Thus, the inversion has replicated the two-dimensional image. However, the more important question is whether the features of the three-dimensional distribution of the ions (j_{ION}) that produced the two-dimensional ENA image have been captured properly by the inversion.

We can answer this question by comparing j_{ION} of our model with the ion intensities of the MSM model. To the right of each image in Fig. 3 are plots of j_{ION} versus L for midnight (0000 MLT), dawn (0600 MLT), noon (1200 MLT), and dusk (1800 MLT). Examination of the MSM plots (upper panel) shows that most of the protons were in the dusk-to-midnight sector with a peak near $L = 3$ and an inner boundary near $L = 2.8$. The dawn sector had the lowest intensities with a narrow peak at $L \cong 4$. The noon sector had the most complex profile with an inner edge at $L \cong 3$ and an outer edge at $L \cong 4$.

The 10-parameter intensity model does not have the flexibility to reproduce the detailed features of the MSM data. For example, because the model is a separable function of L and ϕ, the inner and outer L limits of the ion intensity are constrained to be the same for all ϕ. The effect of this constraint is manifested in the nearly circular, dark polar region of the reconstructed image. Nevertheless, the modeled distribution (lower panel) correctly places the maximum intensities equally in the dusk and midnight sectors; an inner edge is at $L \cong 2.5$ and a peak occurs at $L \cong 3$, in agreement with the MSM intensities. Additional features are correctly extracted, such as the next lower peak intensities in the noon sector and the lowest in the dawn sector.

The parameter extraction was tested on an ideal image with no Poisson counting fluctuations in the pixels (infinite exposure time). However, Roelof, Mauk, and Meier[13] demonstrated that the model and the procedure described previously were stable and robust against degradation due to pixel count fluctuations. Specifically, even when only 30 counts occurred in the brightest pixel (18% fluctuations), the parameters were still extracted to within <10% on average of their proper value.

We conclude that the inversion of a single image successfully extracted the dominant spatial characteristics from the 30-keV proton "data" distribution. The azimuthal asymmetries were found, as well as the peak magnitudes and the approximate positions of the outer and the (not directly visible) inner edges. The simple model was unable to extract more detailed information. To extract finer details from actual measurements, we would (on a real imaging mission) achieve more detail by simultaneously inverting multiple images from sequential viewing positions along the spacecraft orbit. The spatial separation would have to be sufficient so that the images differed significantly. Such a technique would be limited by the time scale for the evolution of the magnetosphere over the exposure time required to acquire the images with acceptable counting statistics. We currently are investigating the optimization of a more detailed model with respect to sequential images and have obtained promising results.

VISUALIZING THE DYNAMICS OF THE MAGNETOSPHERE

We mentioned that image inversion using multiple images to extract finer details of the ion intensity is limited by the dynamic evolution of the magnetosphere. However, this dynamic evolution itself is of great interest. As 30 years of effort has taught us, the global dynamics of the magnetosphere are not easily untangled using *in situ* measurements. Obviously, physically significant cause-and-effect relationships will stand out in magnetospheric images, and their interpretation will not require strict quantitative inversion.

Consequently, the presentation of successive ENA image measurements as a "video" will help scientists to visualize and understand the global magnetospheric evolution. It will also prove helpful in routine data analysis. After all, imaging data are really an interrelated sequence of images, not a set of dissociated independent snapshots.

To demonstrate the usefulness of this concept, we have simulated such a video for the pioneering Swedish imaging microsatellite, Astrid.[14] This tiny spacecraft (25 kg) was launched into a 1000-km circular polar orbit on 24 January 1995. It carried two different ENA cameras (0.1–70 keV surface scattering to a microchannel plate detector and 13–140 keV solid state detector). To simulate the ENA intensities from this low-altitude orbit, we again used the Rice MSM runs for the geomagnetic storm of 22–23 May 1988. This time we used 14-keV O^+ intensities as the basis for our simulation. Figure 4 presents a sequence of three hemispherical pinhole images from a dawn–dusk orbit at magnetic latitudes of 50, 55, and 60°. The left column shows the antisunward view, and the right column shows the sunward view. The limb of the Earth is marked by the white arc. We have added the ENA upward albedo expected for oxygen atoms, which will emerge from the precipitating shower of O^+ dumped downward into the atmosphere during magnetic disturbances. We have estimated the albedo from the calulations of Ishimoto, Romick, and Meng.[15] We have found the orbit videos invaluable in coping with the convoluted three-dimensional structures of the trapped ion populations as viewed "inside-out" from low altitude.

Simulating an ENA image movie by producing every single frame using the MSM and imaging models is computationally prohibitive. To overcome this dif-

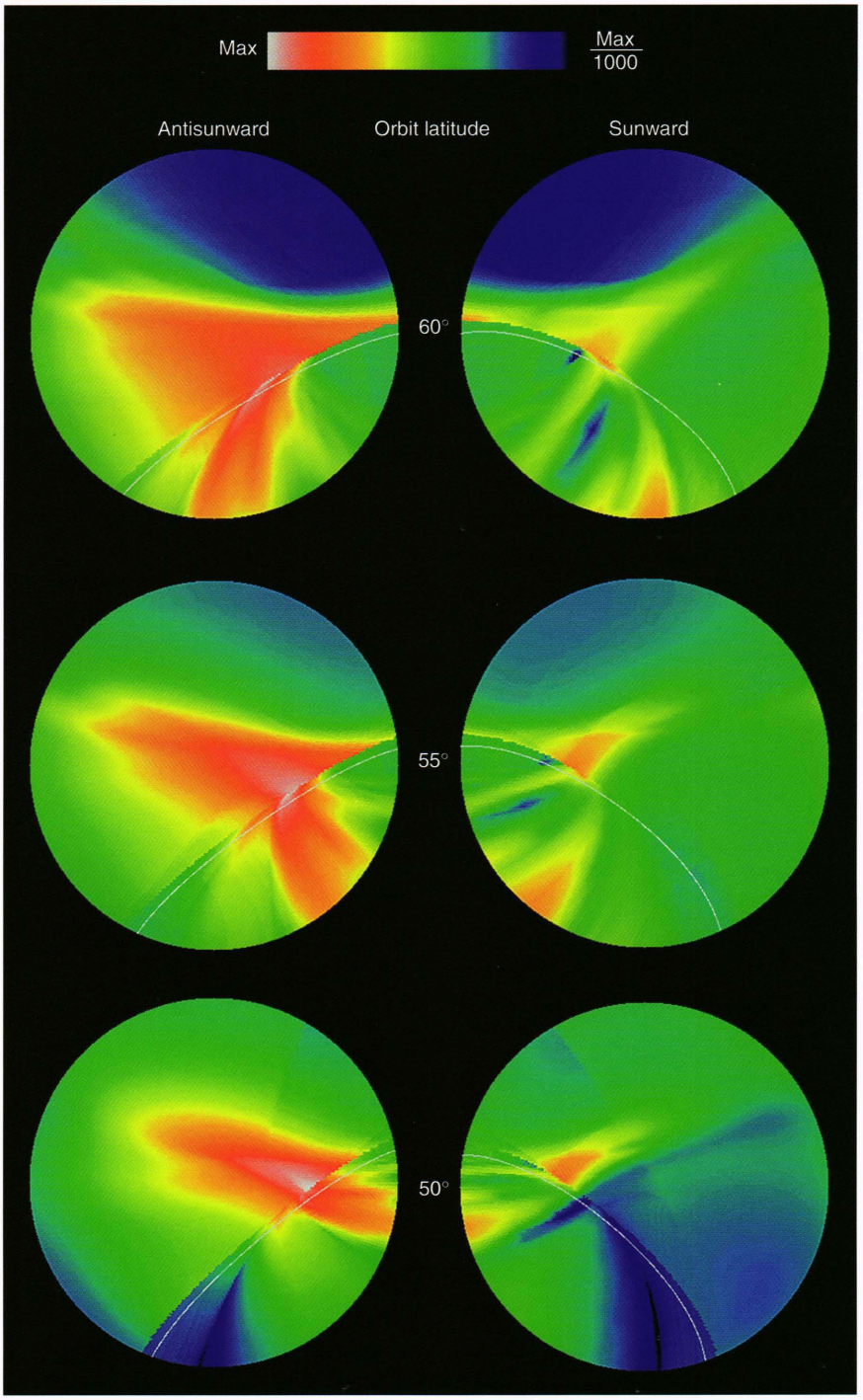

Figure 4. A sequence of three hemispherical pinhole images from a 1000-km dawn–dusk orbit (similar to the Swedish microsatellite, Astrid) at magnetic latitudes of 50, 55, and 60°. The left column shows the antisunward view, and the right column shows the sunward view. The limb of the Earth is marked by the white arc. 14-keV 0^+ intensities were used as the basis of the simulation. "Data" from the MSM plasma computer code for 14-keV 0^+ were also used to calculate upflowing neutral oxygen albedo from precipitating energetic 0^+ during geomagnetic disturbances.

ficulty, only a sequence of sample images was generated from the models. These images were then combined to create a movie by using a popular video editing technique called "morphing." These movies were saved on videocassettes for later study and distribution. Morphing software creates movies from a sequence of images by smoothly varying the features of one image into another. An operator must manually select image features such as boundaries and specially shaped regions. These features are then smoothly deformed from one image to the corresponding features of another. Although complex morphing can be computation and labor intensive, it was considerably more practical than generating each frame directly via the models. For simulation purposes, this approach proved to be effective and practical. The resulting image evolution may not agree with the fine details of the direct approach, but this is neither apparent nor important when viewing the video.

CONCLUSION

This preliminary and exploratory work interpreting magnetospheric images is directed toward setting requirements for future imager designs and for analyzing the streams of images produced. The challenges are great, but the rewards will be grand: visualizations of the global dynamics of the diverse ion populations trapped in the Earth's magnetosphere. After all, these ions are tracers of the electrical fields and currents that permeate the Earth's magnetic field, and EUV and ENA imaging techniques are our only means of "seeing" them.

REFERENCES

[1] Weller, C. S., and Meier, R. R., "First Satellite Observations of the He^+ 304Å Radiation and Its Interpretation," *J. Geophys. Res.* **79**, 1572–1578 (1974).

[2] Roelof, E. C., "Energetic Neutral Atom Image of a Storm-Time Ring Current," *Geophys. Res. Lett.* **14**, 652–655 (1987).
[3] Keath, E. P., Andrews, G. B., Mauk, B. H., Mitchell, D. G., and Williams, D. J., "Instrumentation for Energetic Neutral Atom Imaging of Magnetospheres," in *Solar System Plasma Physics*, Geophysical Monograph 54, American Geophysical Union, Washington, DC, pp. 165–170 (1989).
[4] Hsieh, K. C., and Curtis, C. C., "Remote Sensing of Planetary Magnetospheres: Mass and Energy Analysis of Energetic Neutral Atoms," in *Solar System Plasma Physics*, Geophysical Monograph 54, American Geophysical Union, Washington, DC, pp. 159–164 (1989).
[5] McComas, D. J., Barraclough, B. L., Elphic, R. C., Funsten, H. O., III, and Thomsen, M. F., "Magnetospheric Imaging with Low-Energy Neutral Atoms," *Proc. Natl. Acad. Sci. U.S.A.* **88**, 9598–9602 (1991).
[6] Roelof, E. C., and Williams, D. J., "The Terrestrial Ring Current: From *in situ* Measurements to Global Images Using Energetic Neutral Atoms," *Johns Hopkins APL Tech. Dig.* **9**(2), 144–163 (1988).
[7] Williams, D. J., Roelof, E. C., and Mitchell, D. G., "Global Magnetospheric Imaging," *Rev. Geophys.* **30**, 183–208 (1992)
[8] Rairden, R. L., Frank, L. A., and Craven, J. D., "Geocoronal Imaging with Dynamics Explorer," *J. Geophys. Res.* **91**, 13,613–13,630 (1986).
[9] Chamberlin, J. W., and Hunten, D. H., *Theory of Planetary Atmospheres (2nd Ed.)*, International Geophysics Series, **36**, Academic Press, New York (1987).
[10] Wolf, R. A., Spiro, R. W., and Rich, F. J., "Extension of the Rice Convection Model into the High-Latitude Ionosphere," *J. Atmos. Terr. Phys.* **53**, 817–829 (1991).
[11] Spall, J. C., "Multivariate Stochastic Approximation Using a Simultaneous Perturbation Gradient Approximation," *IEEE Trans. Auto. Control* **37**, 332–341 (1992).
[12] Roelof, E. C., Mauk, B. H., Meier, R. R., Moore, K. R., and Wolf, R. A., "Simulations of EUV and ENA Magnetospheric Images Based on the Rice Convection Model," *Proc. SPIE, Instrumentation for Magnetospheric Imagery II* **2008**, 202–213 (1993).
[13] Roelof, E. C., Mauk, B. H., and Meier, R. R., "Instrument Requirements for Imaging the Magnetophere in Extreme-Ultraviolet and Energetic Neutral Atoms Derived from Computer-Simulated Images," *Proc. SPIE, Instrumentation for Magnetospheric Imagery* **1744**, 19–30 (1992).
[14] Chase, C. J., Mauk, B. H., Roelof, E. C., Wolf, R. A., and Spiro, R. W., "Energetic Neutral Atom Images of H^+ and O^+ Ion Distributions Simulated from *Astrid* 1000 km Polar Orbit," *EOS, Trans. Am. Geophys. Union* **75**, 546 (1994).
[15] Ishimoto, M., Romick, G. J., and Meng, C.-I., "Model Calculation of the N_2^+ First Negative Intensity and Vibrational Enhancement from Energetic Incident O^+ Energy Spectra," *J. Geophys. Res.* **97**, 8653–8660 (1992).

ACKNOWLEDGMENTS: The efforts of both authors were supported in part by NASA Grants NAGW-2619 and NAGW-4140 to APL. Considerable material in this article was developed from collaborative work with our valued APL colleagues Barry H. Mauk, Donald G. Mitchell, and Donald J. Williams.

THE AUTHORS

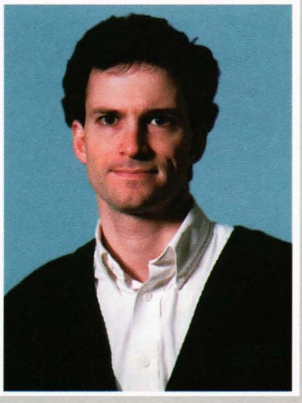

CHRISTOPHER J. CHASE received B.S. degrees in electrical engineering and mathematics from Brigham Young University in 1987, and M.S. and Ph.D. degrees in electrical engineering from Princeton University in 1989 and 1992, respectively. Between 1983 and 1988, he was a member of the Computer Architecture and Sensor System Modeling Departments of The Aerospace Corporation, El Segundo, California. Dr. Chase is now with APL's Computer Science and Technology Group, and he is also an active member of the IEEE. His research interests include dynamical system analysis and control, discrete event systems, communication networks, image processing, parameter estimation, and pattern recognition. His e-mail address is Christopher.Chase@jhuapl.edu.

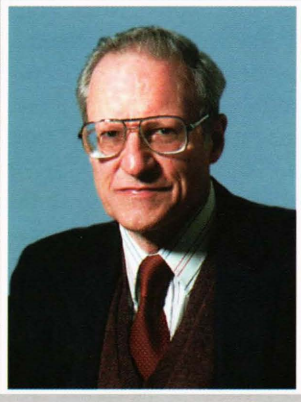

EDMOND C. ROELOF received his Ph.D. in physics from the University of California, Berkeley, in 1966. Before coming to APL, he was a research scientist at the Boeing Scientific Research Laboratories and at the NASA/Goddard Space Flight Center, and later he was an Assistant Professor of Physics at the University of New Hampshire. Dr. Roelof joined APL's Space Physics and Instrumentation Group in 1974. He has held visiting appointments at NOAA's Space Environment Laboratory, as well as at universities and institutes in Europe. He has also served on NASA Management and Operations working groups and as an officer of the American Geophysical Union, from which he received the 1987 Editor's Citation for Excellence in Refereeing (*Geophysical Research Letters*). Dr. Roelof is a coinvestigator for the Ulysses (heliosphere), Galileo (Jupiter), and ISTP (Geotail) missions. His published research covers topics in energetic particles, plasma, magnetic fields, and radio emissions in the solar corona, the interplanetary medium, and the magnetospheres of Earth, Jupiter, and Saturn. His e-mail address is Edmond.Roelof@jhuapl.edu.